Comparison of hydrogen resilience of three different corrosion-resistant martensitic steels

Materials & Design 252 (2025) 113747

Contents lists available at ScienceDirect

Materials & Design

journal homepage: www.elsevier.com/locate/matdes

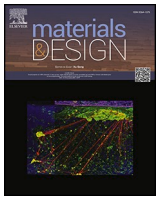

Comparison of hydrogen resilience of three different corrosion-resistant martensitic steels

Severin Jakob [a,*], Mattias Thuvander [a], Steve W. Ooi [b,c]

[a] Department of Physics, Chalmers University of Technology, SE-412 96 Göteborg, Sweden
[b] Maxwell Centre, Ovako Group R&D, JJ Thompson Avenue, Cambridge CB3 0HE, United Kingdom
[c] Ovako Corporate R&D, Building 202, SE-813 82 Hofors, Sweden

ARTICLE INFO

Keywords:
Stainless steel
Hydrogen embrittlement
Hydrogen traps
Atom probe tomography

ABSTRACT

Hydrogen gas is a critical resource for future sustainable energy production, with stainless steels playing a substantial role in applications where components are exposed to hydrogen gas environments. In this work, the resistance to hydrogen embrittlement of three ultra-high strength martensitic stainless steels was investigated. The materials comprised of one high carbon, one nitrogen-alloyed and one dual precipitation hardened steel. The experiments involved a combined deuterium charge, followed by atom probe tomography, and hydrogen gas charge, followed by slow strain rate testing. This approach enabled the study of each steel's resilience to hydrogen gas and allowed correlations between mechanical behaviors after hydrogen charging and their hydrogen trapping capabilities, as well as the presence of undissolved primary carbides or carbonitrides. Results showed that while the nitrogen-alloyed stainless steel demonstrated the highest hydrogen trapping capability, the presence of undissolved primary carbides or carbonitrides within it served as crack initiation sites during slow strain rate tests, reducing its hydrogen resistance. The dual precipitation-hardened steel, which lacked undissolved carbides, exhibited the least hydrogen embrittlement.

1. Introduction

The transition to a fossil-free society and the achievement of global environmental goals hinge on the adoption of green hydrogen as an energy source. However, the future use of hydrogen presents material challenges that must be addressed during the design phase. Hydrogen gas can decompose into atomic hydrogen under high temperatures and pressures in the presence of metal catalysts [1]. This atomic hydrogen can diffuse into steel, preferentially accumulating in areas of high triaxial stress, which promotes crack formation and propagation, which leads to sudden fracture of components exposed to hydrogen environments. This degradation is typically known as hydrogen embrittlement (HE) [2,3]. Hydrogen interacts in the material with vacancies, dislocations, interfaces to second-phase particles as well as lath and grain boundaries [1,4–9]. Several mechanisms have been reported to cause material failure due to hydrogen interaction: hydrogen-enhanced decohesion (HEDE) [10,11], hydrogen-enhanced localized plasticity (HELP) [12,13], hydrogen-enhanced strain-induced vacancies (HESIV) [5], adsorption-induced dislocation emission (AIDE) [14] as well as combinations thereof.

While ultra-high strength steel is recognized for its fatigue properties, hydrogen is known to significantly reduce fatigue life. Consequently, there is an urgent need for ultra-high strength steels that are resistant to the effects of hydrogen environments. HE can be mitigated by the introduction of H traps into the microstructure of the material, since it is only diffusible H that is critical for material failure [2,15,16]. The traps are usually classified according to their strength, i.e. their binding energy. On one hand, lath and grain boundaries may provide abundant trapping sites, but they are weak traps and may release H back into the matrix during operation [17]. On the other hand, nano-sized particles such as different carbides or ε-Cu-precipitates can act as strong traps [18–22]. One method to investigate the actual trapping sites is atom probe tomography (APT) as it offers nearly atomic spatial resolution as well as high sensitivity for all elements, including H [23–27]. H measurement with APT still poses challenges for quantification since H_2 is the main remaining gas molecule in the ultra-high vacuum chamber of the instrument, which is commonly made out of austenitic stainless steel [28–30]. To circumvent this problem, the heavier isotope deuterium (D) can be introduced by electrolytical charging in solutions of heavy water [27,31–33], gas charging [24,25] or ion implantation

* Corresponding author.
E-mail address: severin.jakob@chalmers.se (S. Jakob).

https://doi.org/10.1016/j.matdes.2025.113747
Received 19 November 2024; Received in revised form 13 January 2025; Accepted 19 February 2025
Available online 20 February 2025

Table 1
Measured chemical composition of the investigated steels in wt.-% with Fe as balance.

Material	Alternative designation	C	Si	Mn	Cr	Ni	Mo	V	Al	N
440C	X105CrMo17	1.02	0.8	0.85	16.8	–	0.48	–	–	–
NMS	X40CrMoVN16-2	0.39	0.30	0.25	15.5	–	1.65	0.31	–	0.195
Hybrid 60	X20NiCrAlMoV6-5–2-1	0.28	0.1	0.28	5.61	5.94	0.69	0.49	2.41	–

Table 2
Heat treatment of the three ultra-high strength stainless steels.

Material	Austenitization	Quench	Sub-zero treatment	Tempering/ Aging
440C	1050 °C / 40 min	Oil	−80 °C / 1 h	220 °C / 1 h
NMS	1075 °C / 30 min	Oil	−80 °C / 1 h	2 x 510 °C / 1 h
Hybrid 60	1020 °C / 45 min	Air	n.a.	570 °C / 1 h

[34]. D and H have a similar solubility in steel, and D has a slightly lower diffusivity compared to H. Hence, the mentioned experiments [35,36] are suitable in the investigation of trapping sites in steel. The use of cryogenic transfer has been emphasized since H and D may diffuse and escape the material before measurement [37–39]. It was shown recently that strong enough traps can retain D even after a room temperature transfer, if it is reasonably quick [40]. Transition metal carbides were previously investigated in literature and showed either trapping at the interface [27,41] or within the carbides at C vacancies [25,26]. Recent investigations on mixed metal precipitates show that trapping sites are available within the carbide by either reducing the barrier for in-diffusion of H or increasing the number of C vacancies [42–45].

In this work, three different martensitic stainless steels, that are usually used in the field of bearing applications, were chosen for investigation. The use of stainless steel in applications where the component is in contact with hydrogen is critical since corrosion is also anticipated as water can form due to condensation or due to the reaction of hydrogen with oxygen (air). The steels have similar tensile strength and deformation behavior, however, knowledge about their resilience against HE is lacking. The H trapping and desorption characteristics after hydrogen charging is measured by quantitative thermal desorption mass spectrometry (TDMS). Furthermore, qualitative measurements of trapping sites and D retainment are performed using APT. The mechanical response is characterized by hydrogen gas charging followed by slow strain rate testing (SSRT), and the observed differences between the steels can be explained by the presence (or the lack) of undissolved primary carbides or carbo-nitrides in the materials.

2. Materials and methods

2.1. Materials

Three different martensitic stainless steels; a high carbon martensitic stainless steel (440C), a nitrogen-alloyed martensitic stainless steel (NMS), and a dual precipitation hardening steel (Hybrid 60), were investigated in this study. The measured chemical composition and alternative designations are shown in Table 1. All specimens were machined in soft annealed condition before being heat-treated to achieve a minimum target hardness of 58 HRC. 440C and NMS were oil quenched to room temperature after austenitization and additionally cooled in an ethanol and liquid nitrogen mixture set at −80 °C to transform the remaining austenite to martensite before tempering. Hybrid 60 was air-cooled and does not need sub-zero treatment before aging to achieve peak hardness. The detailed heat treatments can be found in Table 2.

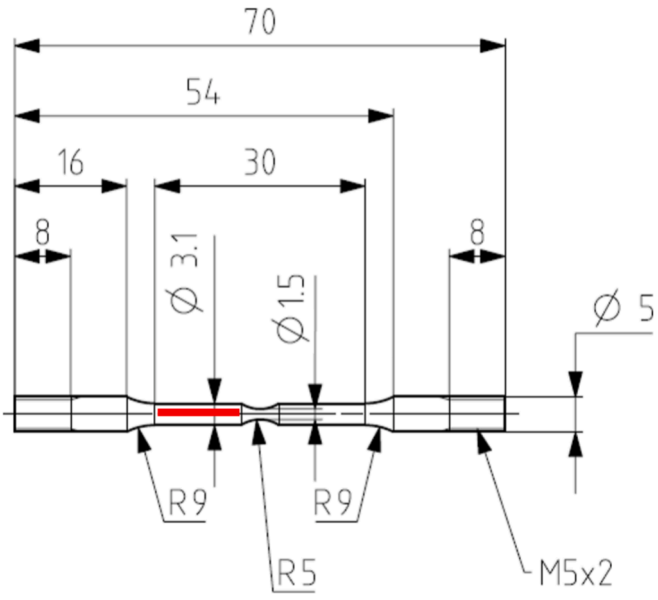

Fig. 1. Sample geometry for SSRT. The APT samples are cut from the shaft of uncharged specimens (highlighted in red). Sinking electric discharged machining was used to create the final 5 mm radius groove in the middle of the SSRT specimens.

2.2. Hydrogen gas charging

All samples were surface-finished by grinding with 600-grit SiC sandpaper and cleaned with isopropanol before hydrogen gas charging. The sample dimensions for hydrogen uptake measurement were 8 x 1 x 60 mm^3 and the hydrogen gas charging was conducted in an autoclave. To reduce the oxygen content, a sequence of pressurizing (80 bar) and degassing cycles was performed seven times. After the oxygen purging, the autoclave was filled with 80 bar hydrogen gas and then inserted into a tube furnace pre-heated to 350 °C. The timing of the hydrogen charging began once a thermocouple attached to the autoclave confirmed that it had reached 350 °C. After the desired exposure time, the autoclave was removed from the furnace and cooled to room temperature before the hydrogen pressure was released. The steel sample (either in plate or in SSRT dimensions) was then extracted and placed in liquid nitrogen to prevent hydrogen diffusion before further testing.

2.3. Thermal desorption mass spectrometry (TDMS)

The hydrogen-charged steel samples were consecutively removed from the liquid nitrogen storage and immersed into ethanol for cleaning and to bring the sample temperature to room temperature. The sample's surface was re-ground using 600-grit sandpaper to eliminate any oxide layer that may have formed during the hydrogen gas charging and was dried with paper towels and compressed air. The sample was then weighed before being placed into the TDMS apparatus, where a heating program was initiated. The heating program involved a controlled heating rate of 1 °C/s, with the sample held at 800 °C for 900 s. TDMS was performed on a Bruker G8 GALILEO.

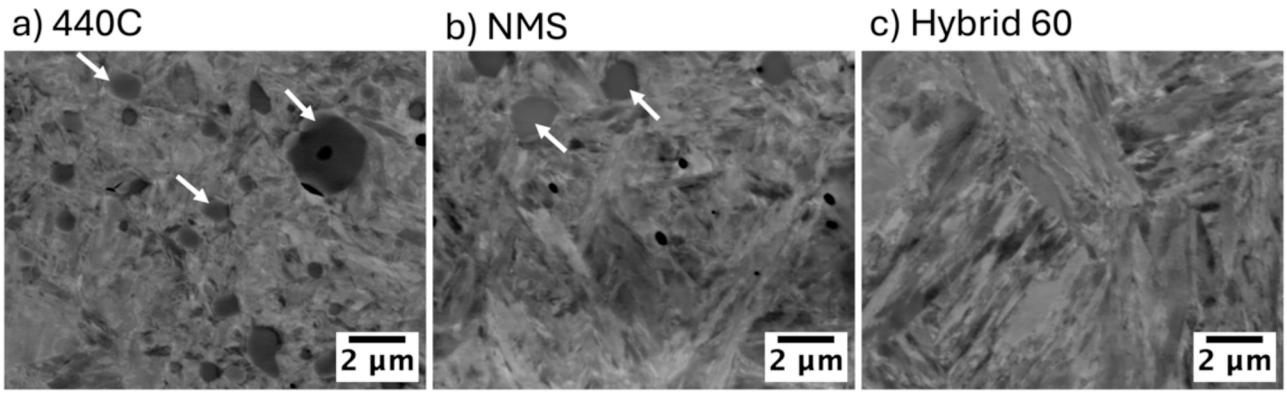

Fig. 2. Microstructures of heat-treated samples. The arrows point out undissolved primary carbides and carbonitrides, respectively.

2.4. Slow strain rate testing (SSRT)

The dimensions of the SSRT samples are shown in Fig. 1. To minimize the impact of high-stress concentration in these ultra-high strength steels, a groove with 5 mm radius was produced by sinking electric discharge machining. This groove pattern reduces localized stress intensities and provides a predefined breaking area.

Samples were measured in their reference state as well as hydrogen gas charged for 24 h as described above. The SSRT testing procedure for charged specimens began by removing the sample from liquid nitrogen and immersing it into ethanol to clean and bring the sample temperature to room temperature. After cleaning, the sample was dried with paper towels and compressed air. The diameter of each sample was measured before placing it in the SSRT setup. A slow extension rate of 0.001 mm/min (1.67 x 10^{-5} mm/s) was applied during testing. Time, load, and crosshead extension were acquired throughout the test.

2.5. Atom probe tomography (APT)

Matchstick samples with dimensions of 0.3 x 0.3 x 12 mm^3 were cut from uncharged SSRT samples for APT needle preparation as shown in Fig. 1. Specimens were electrolytically thinned in a 2-step process in solutions of perchloric acid to achieve sharp tips [23]. APT measurements were performed in voltage-mode with 20 % pulse fraction on a CAMECA LEAP 6000 XR at 70 K test temperature, 200 kHz pulse frequency and 0.3 to 0.5 % detection rate. The reconstructions were performed following the voltage curve within the commercial software AP Suite 6.3. Since the materials are highly alloyed, indications of crystallographic poles are not strong enough for calibration. An image compression factor of 1.53 and a k-factor of 4.7, as calibrated on ferritic steel with nano-scale carbides measured with the same parameters, were used. Cathodic D charging was performed in 0.1 M NaOH in heavy water at 2.2 V against a Pt counter-electrode for 30 s and 3 min, respectively. During measurement in voltage mode no H_2^+ at 2 Da is expected in the

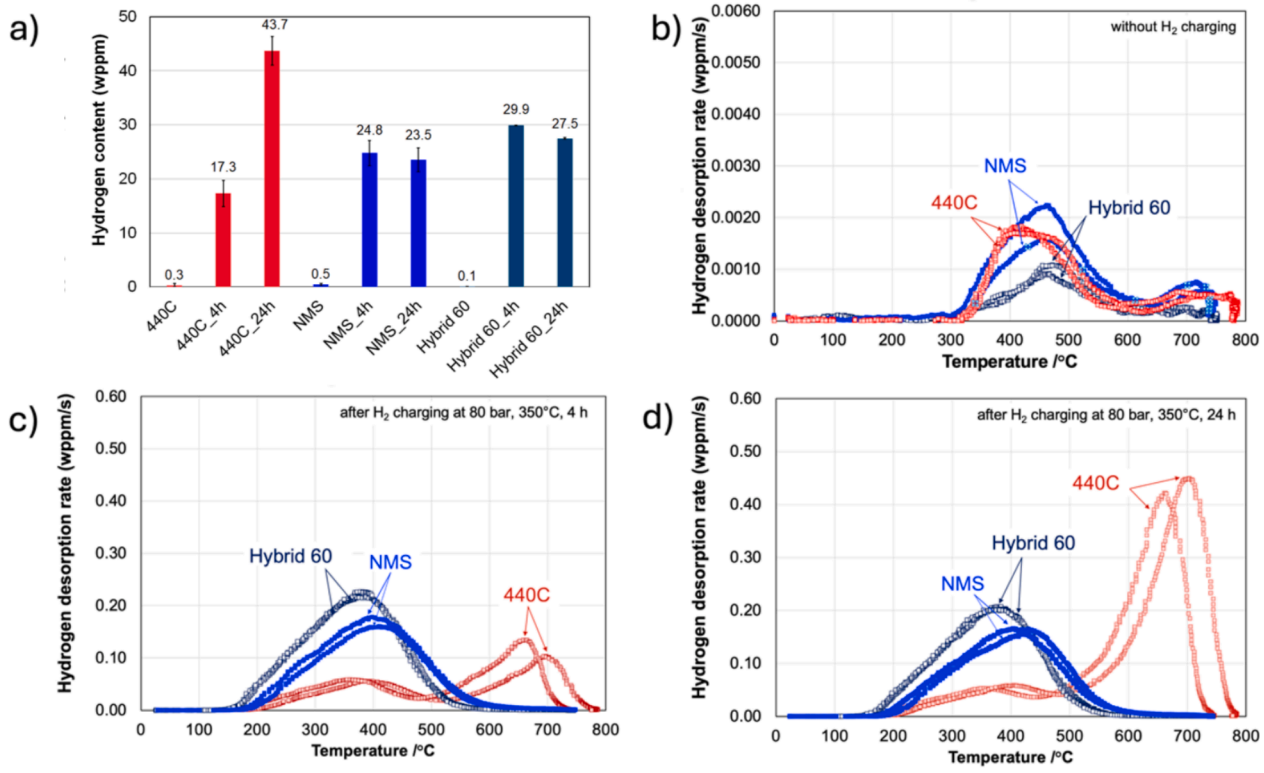

Fig. 3. a) Measured total H content for uncharged specimens and H charged for 4 and24 h with 80 bar H_2 pressure at 350 °C for all three steels; Thermal desorption rates of H for samples b) without H charging, c) after 4 h of charging and d) after 24 h of charging. Note the different scales.

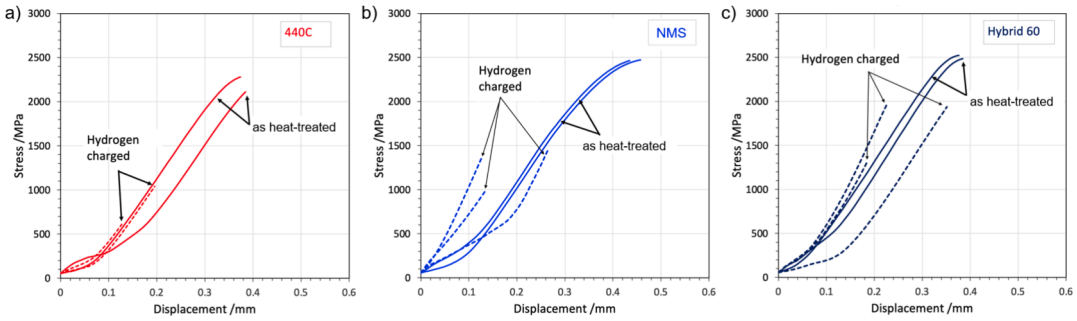

Fig. 4. Engineering stress as a function of crosshead displacement for all SSRT measurements of the three different steels.

mass spectrum due to dissociations in the high electrostatic field. Any counts at 2 Da can therefore be attributed to the electrolytical D charging. Immediately after charging, the specimens were rinsed and dried in N_2 gas flow before loading on a puck and moving the sample through the load-lock and the buffer chamber of the APT instrument. This procedure takes about 15 min to get the specimen to cryogenic temperature in the analysis chamber and it has been shown to retain D in strong enough traps [40]. In total, 5 heat-treated and 10 D charged specimens were successfully measured with 2.2 to 54 million collected ions in each APT run. Mass-spectra with ranges of representative measurements for each material are presented in the supplementary material.

2.6. Results

The resulting microstructures of all three martensitic stainless steels after undergoing heat treatment as presented in Table 2 are depicted in Fig. 2, captured in the scanning electron microscope (SEM) with concentric back-scattered electron mode. All steels exhibit martensitic microstructures. However, undissolved carbides and carbonitrides, ranging from 0.5 to 3 μm in diameter, are observed in 440C (Fig. 2a) and NMS (Fig. 2b), respectively, while no primary carbides are observed in Hybrid 60 (Fig. 2c). These microstructural characteristics align with previous findings in the literature. The investigated steels have been well studied in previous publications and detailed studies on the microstructures of 440C [46–49], NMS [50–53], and Hybrid 60 [54–57] steels can be found elsewhere.

The prevalent carbides that evolved within the martensitic lath in 440C after tempering is cementite. In NMS, carbonitrides of type $M_{23}(C,N)_6$ and M_2X (Mo_2C, Cr_2N) are expected during the final stage of the tempering process. For Hybrid 60, intermetallic NiAl, chromium-rich M_7C_3 and $M_{23}C_6$ and vanadium-rich MC carbide precipitates are expected after tempering at 570 °C. All the precipitates that formed during tempering can only be resolved with either transmission electron microscopy or APT.

TDMS has been performed on the steel samples in uncharged condition as well as after gas charging at 350 °C at 80 bar H_2 pressure for 4 and 24 h. Fig. 3 shows the overall H content (Fig. 3a) and the desorption behavior of the steels (Fig. 3b to d). All materials display a desorption peak of H at temperatures between 200 and 600 °C. Samples of 440C show the lowest amount of desorbed H in this temperature range. However, a second peak between 600 and 800 °C is apparent and an increased H content is detected at a longer charging time for this material. NMS and Hybrid 60 have reached saturation after 4 h of gas charging. These two materials depict similar overall H content, with desorption peaks at slightly higher temperatures for NMS than Hybrid 60.

SSRT is used to evaluate and rank the resistance to HE for the selected stainless steels. By understanding how materials behave under stress after hydrogen gas charging, the material performance and reliability of engineered components in such demanding applications can be guaranteed. Fig. 4 presents the SSRT results for all three materials. The uncharged (as heat-treated) tests are depicted with solid lines and the dashed lines show the SSRT results after H charging. Overall, the curves have the same elastic slope after initial differences due to slight crosshead misalignments. All experiments show HE manifested in the reduced ultimate tensile strength (UTS). The values are averaged in Fig. 5 and an HE index (HEI), calculated according to equation (1) is written above the bars [58].

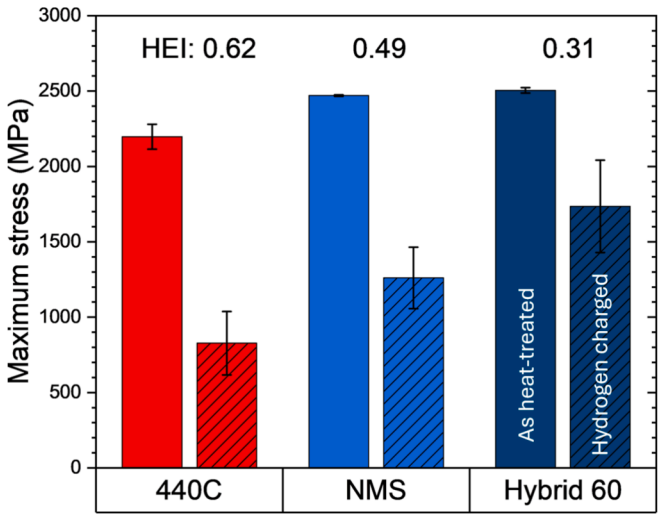

Fig. 5. Maximum stress during SSRT for as heat-treated and H charged conditions. The HE index (HEI) calculated according to equation (1), is written above the columns for each material.

$$HEI = \frac{UTS_{asheat-treated} - UTS_{hydrogencharged}}{UTS_{asheat-treated}} \quad (1)$$

An APT measurement on uncharged 440C included a primary $M_{23}C_6$ particle shown in Fig. 6a. The material contains additional nanometer-sized carbide precipitates. The composition of these (apart from C), as shown in the proxigram in Fig. 6b, does not significantly deviate from the matrix composition due to the low tempering temperature where the diffusivity of substitution atoms is sluggish. Only the run after 3 min charging time shows a D peak for this material and the reconstruction as well as a section of the mass-spectrum are shown in Fig. 6c and d. Due to the severe D charging condition, it is thought that permanent D damage was induced in this material. Here, D_2 molecules may have formed and enabled the detection of D in this charging condition. Notably, the regions with high D content are not connected to the C segregation, highlighted by *iso*-surfaces. Corresponding proxigrams are provided in the supplementary material. Since there are no strong trapping sites in 440C, atomic D would simply desorb from the small APT tip after less severe D charging conditions.

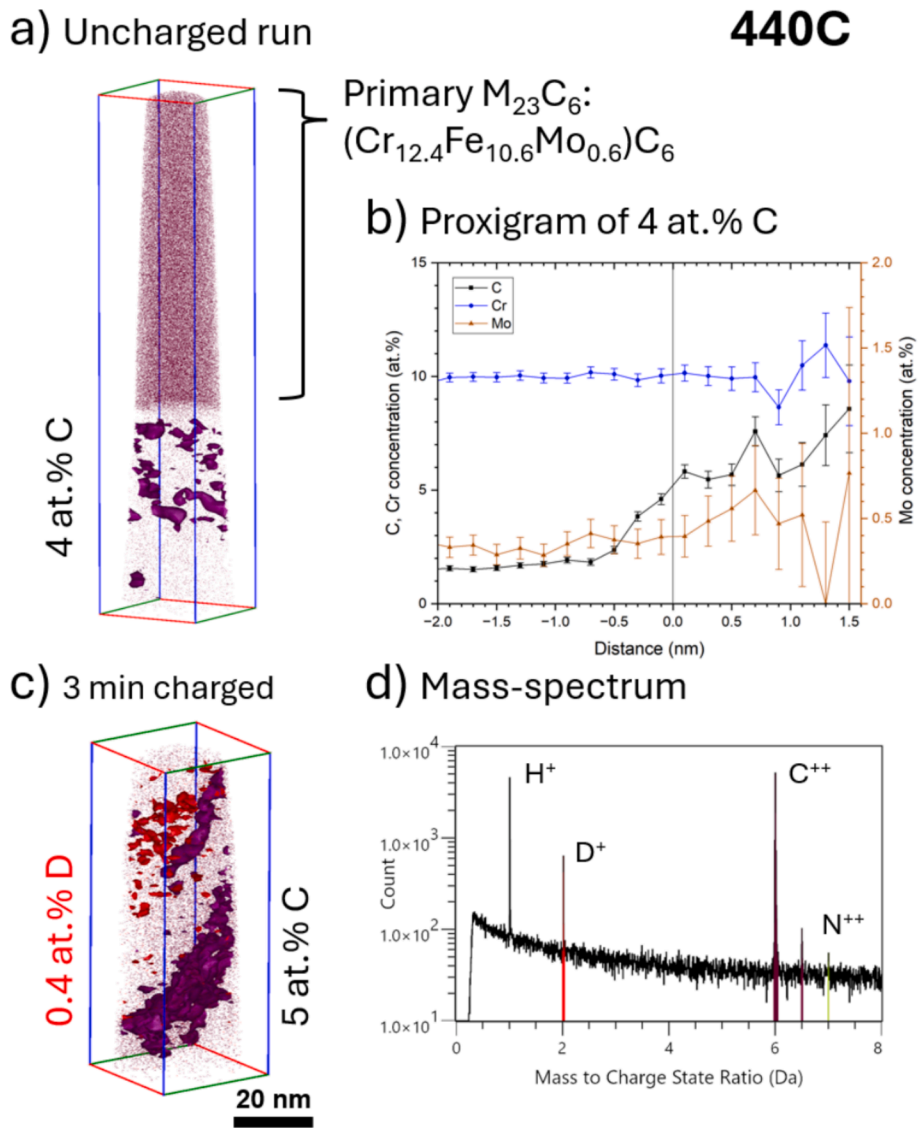

Fig. 6. a) APT reconstruction of an uncharged 440C specimen with a primary $M_{23}C_6$ carbide (top part); only a fraction of the C atoms is shown for visibility. b) shows the proxigram of the 4 at.% C *iso*-surfaces shown in (a); c) APT reconstruction of a 440C specimen after 3 min D charging with C and D *iso*-surfaces and a section of that experiment's mass-spectrum is shown in (d).

Fig. 7 depicts an APT measurement after 30 s D charging from an NMS specimen. D is retained in connection with the Cr-rich $M_{23}(C,N)_6$ precipitates, as displayed by *iso*-surfaces and their proxigram in Fig. 7a and c. The number density and hence the D concentration varies on a local scale, as can be seen by the precipitation-rich section at the top of the reconstruction in comparison to the rest of the measurement. The analysis of lath boundaries (Fig. 7d and e) reveals that carbonitride decorated boundaries trap significant amounts of D whereas less decorated boundaries trap limited amounts. Further APT measurements include N-rich laths as can be seen in the supplementary material.

Fig. 8 depicts the APT measurements of D charged Hybrid 60 specimens. This material is a co-precipitation steel that has intermetallic ß-NiAl particles as well as Cr-rich mixed metal carbides. Three carbide types are present in the material: M_7C_3, $M_{23}C_6$ and sporadic V-rich MC (as seen in an additional run of this material included in the supplementary material). Similar to NMS, carbide decorated lath boundaries, as well as the $M_{23}C_6$ particles, trap D. The slightly larger M_7C_3 retain only a reduced amount of D as can be seen in Fig. 8b.

Fig. 9 presents the overall D concentration for the APT experiments. Specimens of 440C did not retain significant amounts of D above the background noise for a charging time of 30 s. One run with 3 min charging time shows D within the top part of the measurement. This was, however, not connected to the C decorated dislocation lines. NMS is characterized by having high D retainment independent of charging time. Fig. 9b shows the D concentration as a function of C or C + N concentration for a sampling of 100,000 ions for each datapoint along the Z-direction of the APT measurements. The local D concentration can reach values up to 0.6 at.% for NMS specimens. The D concentration is related to the C + N concentrations since the $M_{23}(C,N)_6$ particles are providing the trapping sites in this material. The D concentration in Hybrid 60 is similarly related to the C content from the $M_{23}C_6$ precipitates. The slightly larger M_7C_3 carbides tend to trap significantly less D and can be seen as the extension to the lower right of the enveloping hull lines in Fig. 9b. The linear trendline shows the ratio of D to C or C + N to be 0.14 and is fitting for both NMS and Hybrid 60. Experiments with 3 min D charging time on Hybrid 60 did not yield successful APT runs.

3. Discussion

The hydrogen gas charging temperature (350 °C) is higher than the final tempering temperature applied to the 440C steel, which is expected to cause some softening of the tempered martensite matrix. Since

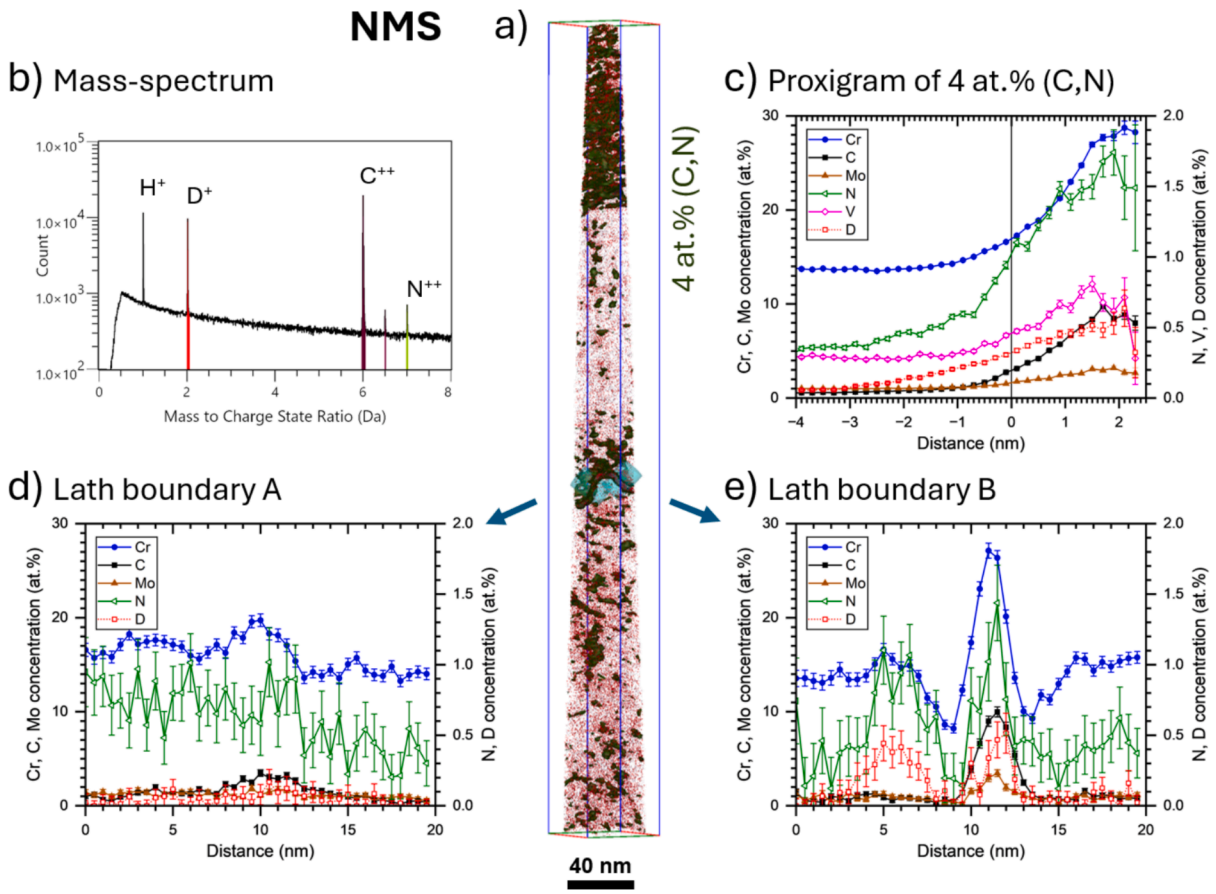

Fig. 7. a) APT reconstruction of a 30 s D charged NMS specimen; D and C atoms as well as 4 at.% (C,N) *iso*-surfaces are displayed. b) shows a selected range of the mass-spectrum. The proxigram of the particles is depicted in (c). d) and e) show 1D concentration profiles from cylindric regions of interest across a less decorated and a carbonitride decorated lath boundary.

softening may also improve ductility, testing was conducted with the aim of comparing 440C with the two other steels tempered at a higher temperature. However, after hydrogen charging, the 440C specimens experienced early breakage during SSRT. The crack was observed to form along the edges of primary carbides (see Fig. 10). This indicates that the matrix softening did not reduce the stress intensity around the primary carbides, nor did it enhance the fracture strength.

Charging has been performed with hydrogen gas for SSRT and TDMS as well as electrolytical charging of D from heavy water solution for APT measurements. While the charging conditions are different, the trapping behavior should be the same since it is a material dependent feature. The hydrogen gas needs to be decomposed into atomic H before it can diffuse into the steel. Differences in diffusivity of H vs. D are small and hence negligible [35]. Only trapping sites that have a saddle energy to enter, may be filled at the higher temperature during gas charging as opposed to electrolytical charging [24]. Consequently, these traps would have a higher de-trapping energy as well. Due to the small size of an APT specimen, the analyzed volume should already be saturated after 30 s of D charging. A recent publication showed no influence of charging time on the amount of trapped H [62].

Stoichiometric cementite has a high energy barrier for in-diffusion of H and (weak) trapping occurs at the interface [63]. Only deformed cementite with increased number of C vacancies showed trapping within cementite lamella of perlite [64,65]. Some hydrogen is desorbed during TDMS of 440C at similar temperatures as the other steels, which may come from primary $M_{23}C_6$, as observed by APT in Fig. 6a. The detection of high-temperature hydrogen desorption and the continuous increase in spectrum intensity (indicative of desorbed quantity) with increasing charging duration during TDMS analysis of 440C steel can be attributed to i) the formation of hydrogen molecules (H_2) or ii) the formation of methane (CH_4) due to the reaction between hydrogen and carbon within cementite precipitates during hydrogen charging (80 bar and 350 °C). Hydrogen molecule formation in 440C steel may result from the high volume fraction of large primary carbides, which could result in the high density of 'wide' carbide and matrix interfaces that facilitate hydrogen molecule (H_2) formation. Methane formation can also occur when hydrogen enters cementite-containing steel at elevated temperatures (>250 °C), a phenomenon often associated with so-called 'Hydrogen Attack' [59–61]. However, due to the high strength of the 440C martensitic matrix, this does not lead to bubble formation. The formation of both H_2 and CH_4 most probably contributes to the observed high-temperature hydrogen desorption during TDMS analysis.

The TDMS experiments show a similar desorption peak between 200 and 600 °C for NMS as well as Hybrid 60. The peak is shifted to slightly higher temperatures for NMS (Fig. 3b). This means that the carbonitride $M_{23}(C,N)_6$ particles in NMS have stronger trapping sites than $M_{23}C_6$ in Hybrid 60. Higher concentrations of D are similarly retained in APT experiments for NMS than for Hybrid 60, as can be seen in Fig. 9a. The local concentrations of D are limited to about 0.15 at.% for $M_{23}C_6$, whereas $M_{23}(C,N)_6$ has local concentrations up to 0.6 at.% (Fig. 9b). From the proxigrams in Fig. 7c and Fig. 8d one can see that the particles trap D to a slightly different extent. On one hand, $M_{23}C_6$ in Hybrid 60 has a D concentration of about 0.6 at.% within the particles and 0.2 at.% at the *iso*-surfaces. On the other hand, $M_{23}(C,N)_6$ in NMS have a similar D concentration within the particle, but a higher concentration of 0.4 at.% at the *iso*-surfaces. This indicates that the interface, where a mismatch between the matrix lattice and the particle's crystal structure has to be accommodated, is a better trapping site in case of carbonitrides. Fig. 8b

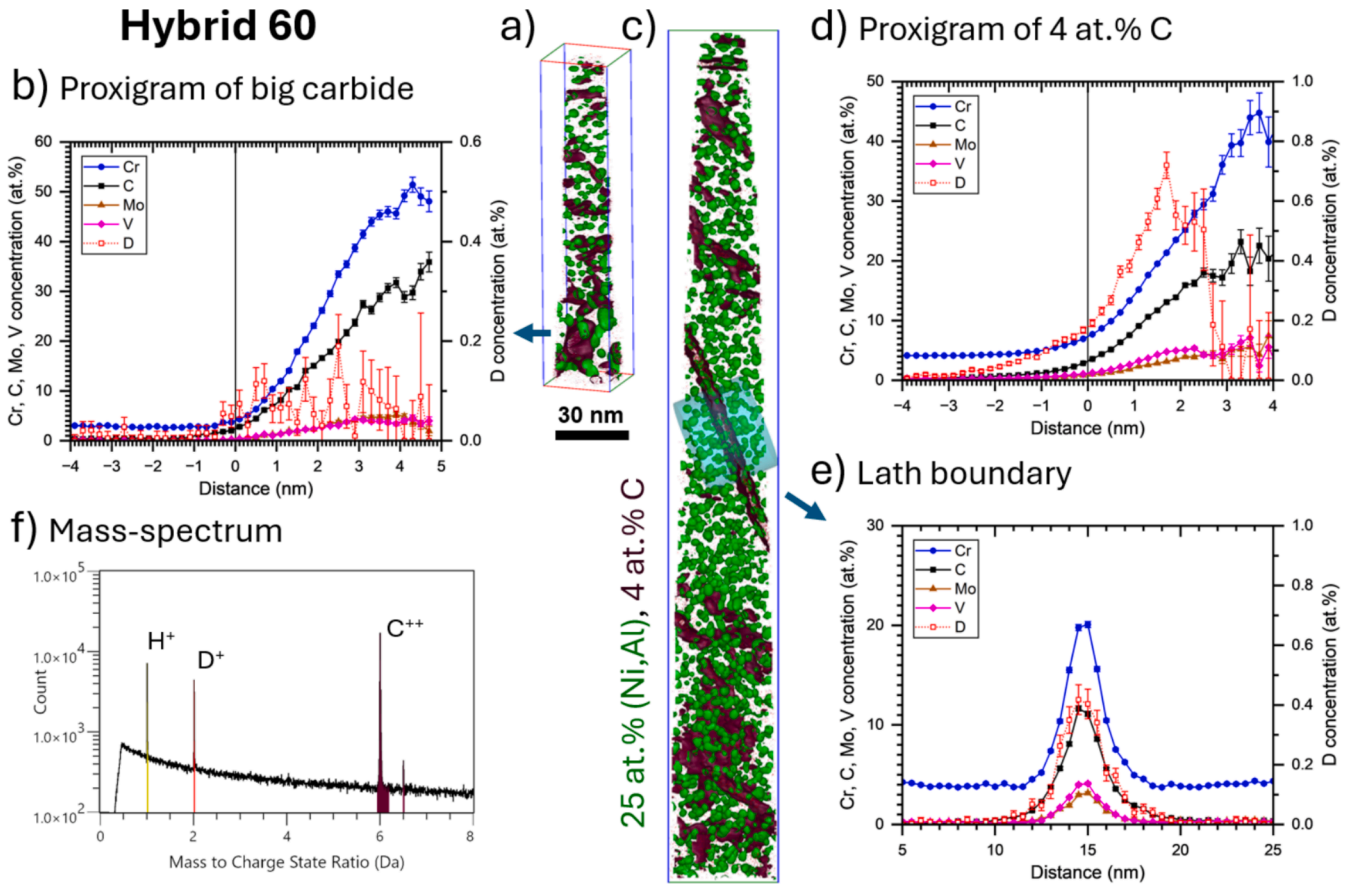

Fig. 8. a) and c) show APT reconstructions of D charged Hybrid 60 specimens with 4 at.% C and 25 at.% (Ni,Al) *iso*-surfaces to highlight the precipitates. b) depicts the proxigram of an M_7C_3 carbide shown in (a). c) shows the APT reconstruction of a successful D charged experiment with connected information: d) Proxigram of 4 at.% C *iso*-surfaces, e) 1D concentration profile through a carbide decorated lath boundary and f) section of the mass-spectrum. Note the different scales for the D concentrations.

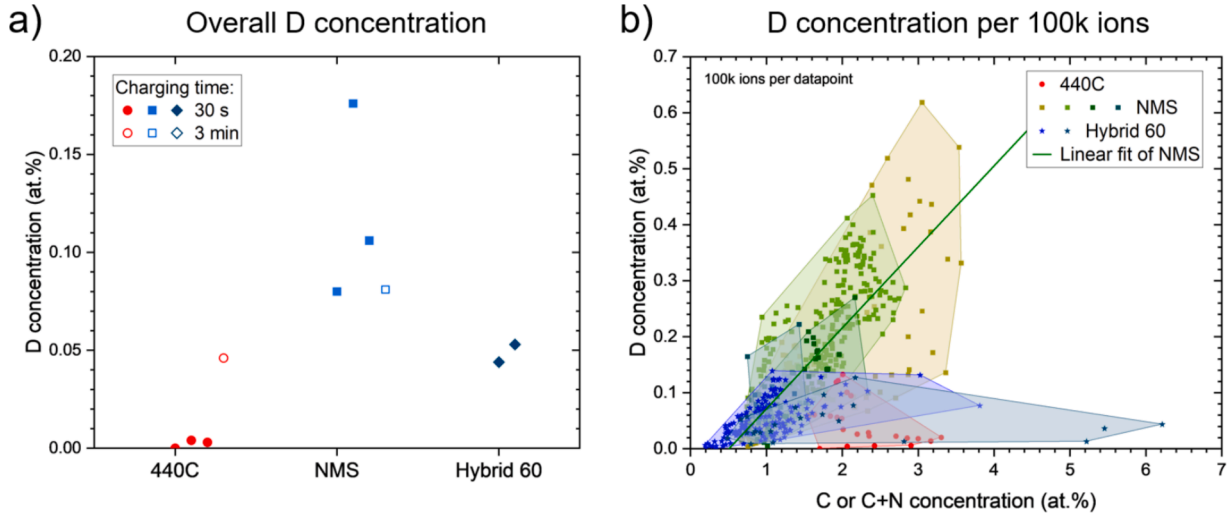

Fig. 9. a) Overall background-corrected D concentration in the APT runs; b) depicts the D concentration as a function of C or (C,N) concentration with a sampling of 100,000 ions each. For more details see the text.

shows the proxigram of a slightly larger carbide in Hybrid 60. It is seemingly an M_7C_3 particle as indicated by the C concentration. D is trapped inside the particle to a limited extent of about 0.1 at.%. The D concentration in the carbide proxigram of Hybrid 60, as depicted in Fig. 8d, decreases for higher distance from the *iso*-surface, i.e. the core region of large carbides traps less D. This could come from sampling slightly larger M_7C_3 particles with less trapping sites or that the core region of larger $M_{23}C_6$ precipitates do not offer trapping sites or have an energy barrier for in-diffusion of D.

440C has the worst D trapping capabilities as investigated by TDMS and APT experiments (Fig. 3 and Fig. 9). It also shows the highest extent of HE as can be seen from the SSRT experiments in Fig. 5. NMS and

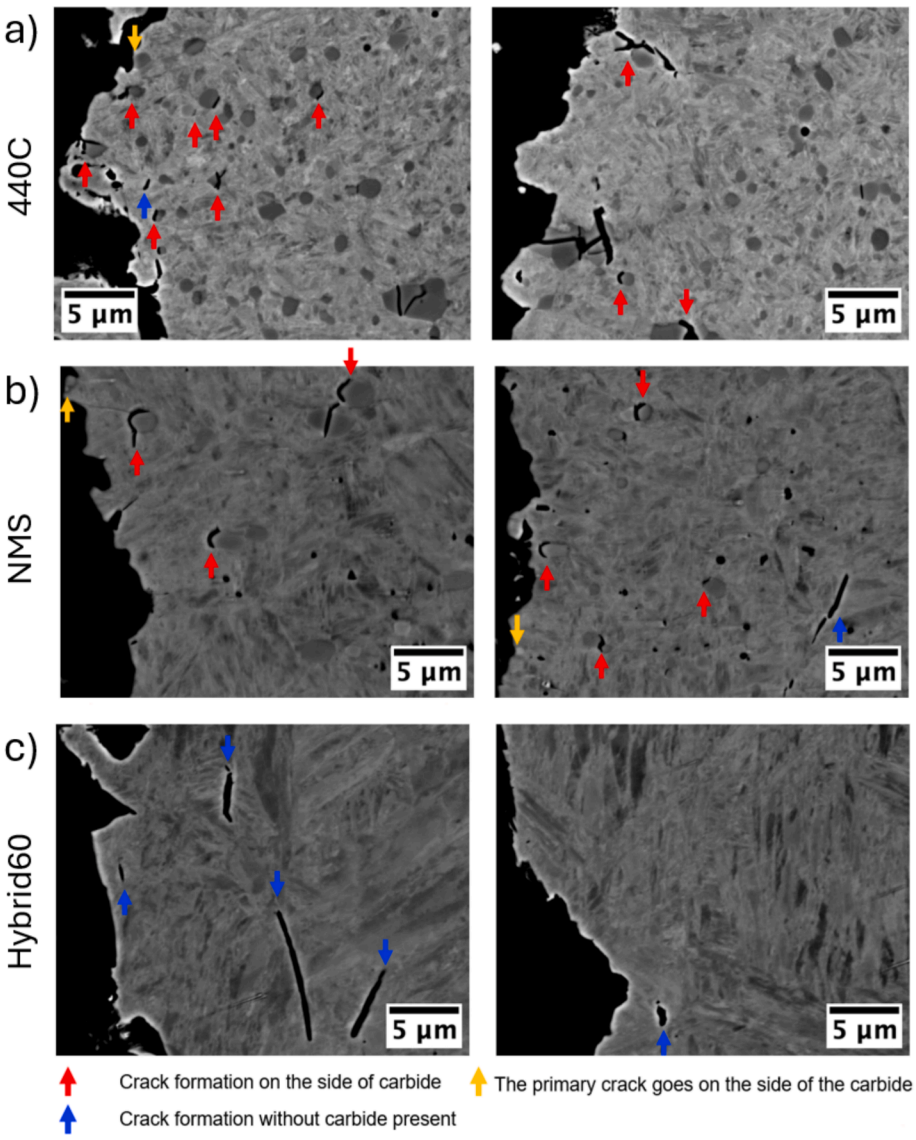

Fig. 10. SEM images of cross-sections near the fracture surfaces of H-charged SSRT samples. 440C and NMS have cracks at primary carbides and carbonitrides, respectively. The spherical dark holes are due to the carbide drop-off (pull out) during polishing.

Hybrid 60 trap similar amounts of H and the traps are already saturated after 4 h of charging as can be seen in Fig. 3a. The majority of the trapping sites are in both cases related to the $M_{23}C_6$ and $M_{23}(C, N)_6$ precipitates, respectively. The traps in NMS are slightly stronger than in Hybrid 60 as can be seen in Fig. 3b. The APT experiments confirm the strong trapping in NMS as more D is retained for this material than for Hybrid 60 (see Fig. 9). However, Hybrid 60 performed better than NMS in the SSRT experiments as depicted in Fig. 5. Thus, the reason for the better hydrogen resilience of Hybrid 60 in comparison to NMS cannot be found in the different trapping capabilities of the materials.

Fig. 10 and Fig. 11 show SEM micrographs of cross-sections near the fracture surface of H charged and as heat-treated SSRT specimens, respectively. Besides the primary crack that led to the failure of the sample, several secondary cracks are visible. In the cases of 440C and NMS (Fig. 10a and b), the primary crack is also formed along a particle interface and most secondary cracks appear at the interfaces of the primary carbides and carbonitrides, respectively. Furthermore, cracks appear within the larger carbides of 440C (see Fig. 10a and Fig. 11a). Cracks also appear at primary carbides and carbonitrides in 440C and NMS for the as heat-treated condition (Fig. 11a and c). The large (elongated) carbide in 440C, as depicted in Fig. 11a, appears to crack under tensile stress. However, this large (elongated) carbide does not crack in the investigated area further away from the crack surface, as can be seen in Fig. 11b. This can be explained by excessive deformation near the fracture area during SSRT. Hybrid 60 appears to contain no large carbides (Fig. 10c and Fig. 11d), and all secondary cracks appear to be located at lath/grain boundaries. The serrated crack line further indicates separation at these interfaces.

HE is caused by the diffusible hydrogen that concentrates in high triaxial stress regions in steel [66,67]. While dislocations and grain boundaries are reported to trap H [1,2,4], the trapping energy of both are too low to delay/prevent HE. Furthermore, dislocations and grain boundaries can also promote diffusion, it is known that dislocation cores promote high diffusivity [1]. So, for ferritic/martensitic steel, discussing the presence of dislocations and grain boundaries in HE prevention is irrelevant. The incoherent boundary between inclusions and matrix is known to trap hydrogen as hydrogen molecules (gas) [68,69]. The presence of inclusions is beneficial only if the H supply is limited, because this allows the trapping of H as gas at the inclusion interphase. However, the large amount of continuous supply of H promotes hydrogen-induced cracking from the inclusion [70,71]. Martensitic/bainitic steels may contain small amounts of remaining/retained

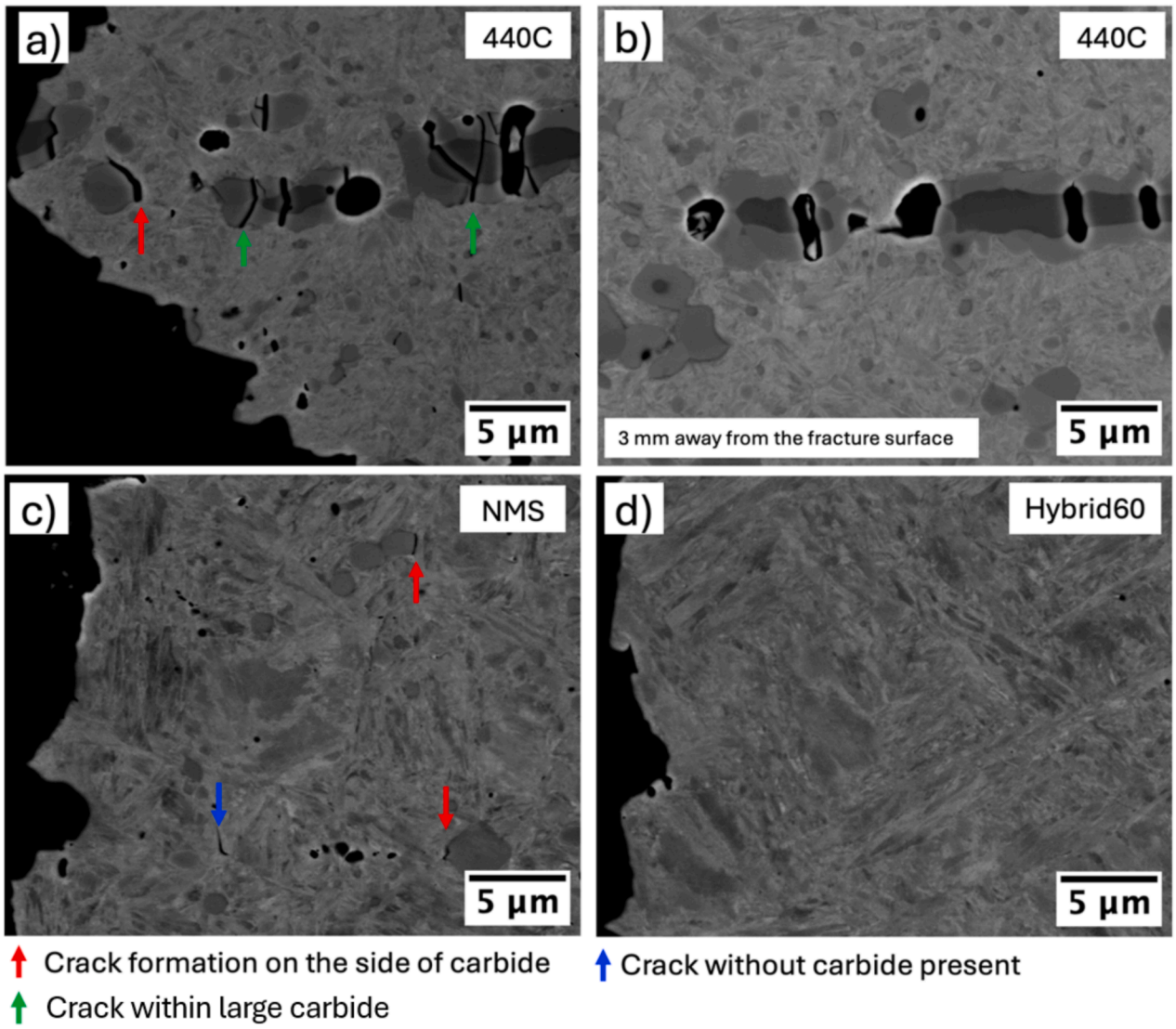

Fig. 11. SEM images of cross-sections near the fracture surfaces of SSRT specimens in as heat-treated condition. The spherical dark holes are due to the carbide drop-off (pull out) during polishing.

austenite. The solubility of H in austenite is higher, and the diffusivity of the H in austenite is a few orders of magnitude slower than in the ferrite/bainite/martensite phase [2]. Austenite can potentially act as trapping site. However, if it is destabilized by H and stress, it will also supply the matrix with diffusible H, which promotes failure [72–74].

We see a reduction in tensile strength for all three steels. The H concentration in the matrix is in a dynamic equilibrium of trapping and de-trapping. While more experimental work is needed for confirmation, it is a reasonable assumption that trapped H may also become mobile under an externally applied stress. The diffusion of escaped H to high stress regions would then promote crack formation. The reduction in fracture strength of 440C is primarily due to the promotion of crack formation at the primary carbide edges (perpendicular to the tensile direction), exacerbated by presence of H due to the combined effects of stress and H molecule (gas) formation at the carbide and matrix interphase. Similarly, the stress concentrations near the large primary carbonitrides in NMS are the primary cause of the reduction in tensile strength under H charged conditions. Hybrid 60 has apparently no undissolved primary carbides and hence can withstand higher tensile loading.

4. Conclusion

In this work, high carbon (440C), nitrogen-alloyed (NMS), and dual precipitation hardening (Hybrid 60) martensitic stainless steels were investigated for their hydrogen resilience. Thermal desorption mass spectrometry showed similar trapping capabilities for NMS and Hybrid 60, with stronger trapping in NMS. 440C displayed high amounts of desorbed H at high temperatures, suggesting H_2 molecule or methane formation. Atom probe tomography measurements with cathodically D charged specimens were performed to qualitatively measure D content and reveal trapping sites in the ultra-high-strength stainless steels. A large, undissolved primary carbide was detected in 440C as well as smaller tempered cementite precipitates, that do not trap D. The trapped D detected in NMS is related to the $M_{23}(C,N)_6$ precipitates as well as carbonitride decorated lath boundaries. Similarly, the trapped D in Hybrid 60 is detected to be close to $M_{23}C_6$ precipitates, whereas the slightly larger M_7C_3 particles were observed to be less effective in trapping D. Atom probe measurements confirm higher D trapping in NMS than in Hybrid 60. In contrast to H trapping experiments, the slow strain rate testing shows the best hydrogen resilience for Hybrid 60, followed by NMS and 440C. This could be explained by the presence of primary carbides and carbonitrides in both steels. Cracking at the

interface between these large particles and the matrix was observed on cross-sections near the fracture surface, indicating the combined effect of H and stress in promoting crack formation. Hybrid 60 appears to have no undissolved primary carbides and thus did not suffer from these high-stress concentration regions. The reduction of tensile strength and formation of cracks in the investigated steels after H gas charging indicate that the trapped H may become mobile under mechanical stress.

CRediT authorship contribution statement

Severin Jakob: Writing – original draft, Visualization, Methodology, Investigation, Formal analysis, Data curation, Conceptualization. **Mattias Thuvander:** Writing – review & editing, Validation, Supervision, Project administration, Funding acquisition, Conceptualization. **Steve W. Ooi:** Writing – review & editing, Writing – original draft, Visualization, Validation, Supervision, Project administration, Investigation, Funding acquisition, Data curation, Conceptualization.

Declaration of competing interest

The authors declare that they have no known competing financial interests or personal relationships that could have appeared to influence the work reported in this paper.

Acknowledgments

The research is partly funded by the Swedish Research Council (2021-05072) and Ovako AB. The APT measurements were performed at Chalmers Materials Analysis Laboratory (CMAL). The TDMS and SSRT measurements were performed at Swerim AB.

Appendix A. Supplementary data

Supplementary data to this article can be found online at https://doi.org/10.1016/j.matdes.2025.113747.

Data availability

Data will be made available on request.

References

[1] A. Turnbull, *Hydrogen diffusion and trapping in metals*. Cambridge: Woodhead Publishing Limited, 2012.,Cambridge.
[2] H.K.D.H. Bhadeshia, *ISIJ Int.*, 56 (1) (2016) 24–36, https://doi.org/10.2355/isijinternational.ISIJINT-2015-430.
[3] X. Li, J. Zhang, Y. Cui, M.B. Djukic, H. Feng, Y. Wang, *Int. J. Hydrogen Energy* 72 (2024) 74–109, https://doi.org/10.1016/j.ijhydene.2024.05.257.
[4] R.A. Oriani, *Acta Metall.*, 18 (1) (1970) 147–157, https://doi.org/10.1016/0001-6160(70)90078-7.
[5] M. Nagumo, K. Takai, *Acta Mater.*, 165 (2019) 722–733, https://doi.org/10.1016/j.actamat.2018.12.013.
[6] Y. Sugiyama, N. Kurihara, Y. Matsumoto, K. Takai, *Scr. Mater.*, 202 (2021) 114031, https://doi.org/10.1016/j.scriptamat.2021.114031.
[7] A. Barnoush, H. Vehoff, *Acta Mater.*, 58 (16) (2010) 5274–5285, https://doi.org/10.1016/j.actamat.2010.05.057.
[8] S. Wang, M.L. Martin, P. Sofronis, S. Ohnuki, N. Hashimoto, I.M. Robertson, *Acta Mater.*, 69 (2014) 275–282, https://doi.org/10.1016/j.actamat.2014.01.060.
[9] S. Wang, M.L. Martin, I.M. Robertson, P. Sofronis, *Acta Mater.*, 107 (2016) 279–288, https://doi.org/10.1016/j.actamat.2016.01.067.
[10] R.A. Oriani, P.H. Josephic, *Acta Metall.*, 22 (9) (1974) 1065–1074, https://doi.org/10.1016/0001-6160(74)90061-3.
[11] T. A. R., *Trans. ASM*, vol. 52, pp. 54–81, 1960, Accessed: Jan. 09, 2025. [Online]. Available: https://cir.nii.ac.jp/crid/1570009751286220288.bib?lang=en.
[12] H.K. Birnbaum, P. Sofronis, *Mater. Sci. Eng. A* 176 (1–2) (1994) 191–202, https://doi.org/10.1016/0921-5093(94)90975-X.
[13] J. Song, W.A. Curtin, *Acta Mater.*, 68 (2014) 61–69, https://doi.org/10.1016/j.actamat.2014.01.008.
[14] S.P. Lynch, *Acta Metall.*, 36 (10) (1988) 2639–2661, https://doi.org/10.1016/0001-6160(88)90113-7.
[15] T.I. Ramjaun, S.W. Ooi, R. Morana, H.K.D.H. Bhadeshia, *Mater. Sci. Technol.*, 34 (14) (2018) 1737–1746, https://doi.org/10.1080/02670836.2018.1475919.
[16] W.H. Johnson, *R. Soc.*, 23 (May) (1875) 168–179.
[17] J. Venezuela, Q. Zhou, Q. Liu, H. Li, M. Zhang, M.S. Dargusch, A. Atrens, *Mater. Today Commun.*, 17 (2018) 1–14, https://doi.org/10.1016/J.MTCOMM.2018.07.011.
[18] H.G. Lee, J.Y. Lee, *Acta Metall.*, 32 (1) (1984) 131–136, https://doi.org/10.1016/0001-6160(84)90210-4.
[19] C. Zhang, Y. Liu, C. Jiang, J. Xiao, *J. Iron Steel Res. Int.*, 18 (6) (2011) 49–53, https://doi.org/10.1016/S1006-706X(11)60077-0.
[20] H. Asahi, D. Hirakami, S. Yamasaki, *ISIJ Int.*, 43 (4) (2003) 527–533, https://doi.org/10.2355/isijinternational.43.527.
[21] D. Li, R.P. Gangloff, J.R. Scully, *Metall Mater. Trans. A Phys. Metall. Mater. Sci.*, 35 A, 3 (2004) 849–864, https://doi.org/10.1007/s11661-004-0011-1.
[22] Y.C. Lin, I.E. McCarroll, Y.T. Lin, W.C. Chung, J.M. Cairney, H.W. Yen, *Acta Mater.*, 196 (2020) 516–527, https://doi.org/10.1016/j.actamat.2020.06.046.
[23] W. Lefebvre-Ulrikson, F. Vurpillot, and X. Sauvage, *Atom Probe Tomography: Put Theory Into Practice*. London: Academic Press, 2016., London.
[24] J. Takahashi, K. Kawakami, Y. Kobayashi, T. Tarui, *Scr. Mater.*, 63 (3) (2010) 261–264, https://doi.org/10.1016/j.scriptamat.2010.03.012.
[25] J. Takahashi, K. Kawakami, T. Tarui, *Scr. Mater.*, 67 (2) (2012) 213–216, https://doi.org/10.1016/j.scriptamat.2012.04.022.
[26] Y.S. Chen, D. Haley, S.S.A. Gerstl, A.J. London, F. Sweeney, R.A. Wepf, W. M. Rainforth, P.A.J. Bagot, M.P. Moody, *Science (80-.).*, 355 (6330) (2017) 1196–1199, https://doi.org/10.1126/science.aal2418.
[27] Y.S. Chen, H. Lu, J. Liang, A. Rosenthal, H. Liu, G. Sneddon, I. McCarroll, Z. Zhao, W. Li, A. Guo, J.M. Cairney, *Science (80-.).*, 367 (6474) (2020) 171–175, https://doi.org/10.1126/science.aaz0122.
[28] B. Gault, et al., *Microsc. Microanal.*, 00 (2024) 1–16, https://doi.org/10.1093/mam/ozae081.
[29] G. Sundell, M. Thuvander, H.O. Andrén, *Ultramicroscopy* 132 (2013) 285–289, https://doi.org/10.1016/j.ultramic.2013.01.007.
[30] Y.S. Chen, P.Y. Liu, R. Niu, A. Devaraj, H.W. Yen, R.K.W. Marceau, J.M. Cairney, *Microsc. Microanal.*, 29 (1) (2023) 1–15, https://doi.org/10.1093/micmic/ozac005.
[31] D. Haley, S.V. Merzlikin, P. Choi, D. Raabe, *Int. J. Hydrogen Energy* 39 (23) (2014) 12221–12229, https://doi.org/10.1016/j.ijhydene.2014.05.169.
[32] A.J. Breen, L.T. Stephenson, B. Sun, Y. Li, O. Kasian, D. Raabe, M. Herbig, B. Gault, *Acta Mater.*, 188 (2020) 108–120, https://doi.org/10.1016/j.actamat.2020.02.004.
[33] I.E. McCarroll, Y.C. Lin, A. Rosenthal, H.W. Yen, J.M. Cairney, *Scr. Mater.*, 221 (June) (2022) 114934, https://doi.org/10.1016/j.scriptamat.2022.114934.
[34] H. Takamizawa, K. Hoshi, Y. Shimizu, F. Yano, K. Inoue, S. Nagata, T. Shikama, and Y. Nagai, *Appl. Phys. Express*, vol. 6, no. 6, 2013, doi: 10.7567/APEX.6.066602.
[35] Y. Hayashi, H. Hagi, A. Tahara, Zeitschrift Fur Phys. *Chemie* 164 (Part_1) (1989) 815–820, https://doi.org/10.1524/zpch.1989.164.Part_1.0815.
[36] W. Raczynski, *Phys. Status Solidi* 48 (1978) K27–K30, https://doi.org/10.1002/pssa.2210480143.
[37] L.T. Stephenson, A. Szczepaniak, I. Mouton, K.A.K. Rusitzka, A.J. Breen, U. Tezins, A. Sturm, D. Vogel, Y. Chang, P. Kontis, A. Rosenthal, J.D. Shepard, U. Maier, T. F. Kelly, D. Raabe, B. Gault, *PLoS One* 13 (12) (2018) 1–13, https://doi.org/10.1371/journal.pone.0209211.
[38] J.M. Cairney, I. McCarroll, Y.-S. Chen, K. Eder, T. Sato, Z. Liu, A. Rosenthal, R. Wepf, *Microsc. Microanal.*, 25 (S2) (2019) 2494–2495, https://doi.org/10.1017/s1431927619013205.
[39] I.E. McCarroll, P.A.J. Bagot, A. Devaraj, D.E. Perea, J.M. Cairney, *Mater. Today Adv.*, 7 (2020) 100090, https://doi.org/10.1016/j.mtadv.2020.100090.
[40] S. Jakob, M. Sattari, B. Sefer, S. Ooi, M. Thuvander, *Scr. Mater.*, 243 (2024) 115963, https://doi.org/10.1016/j.scriptamat.2023.115963.
[41] R. Shi, Y. Ma, Z. Wang, L. Gao, X.S. Yang, L. Qiao, X. Pang, *Acta Mater.*, 200 (2020) 686–698, https://doi.org/10.1016/j.actamat.2020.09.031.
[42] J. Lee, T. Lee, D.J. Mun, C.M. Bae, C.S. Lee, *Sci. Rep.*, 9 (1) (2019) 1–9, https://doi.org/10.1038/s41598-019-41436-2.
[43] M. Kameya, S. Taniguchi, Y. Kobayashi, N. Matsui, S. Yamasaki, *Tetsu-to-Hagane/journal Iron Steel Inst. Japan* 109 (4) (2023) 301–310, https://doi.org/10.2355/TETSUTOHAGANE.TETSU-2022-090.
[44] M. Moshtaghi, E. Maawad, A. Bendo, A. Krause, J. Todt, J. Keckes, M. Safyari, *Mater. Des.*, 234 (July) (2023) 112323, https://doi.org/10.1016/j.matdes.2023.112323.
[45] P. Liu, B. Zhang, R. Niu, S.-L. Lu, C. Huang, M. Wang, F. Tian, Y. Mao, T. Li, P. A. Burr, H. Lu, A. Guo, H.-W. Yen, J.M. Cairney, H. Chen, Y.-S. Chen, *Nat. Commun.*, 15 (724) (2024) 1–13, https://doi.org/10.1038/s41467-024-45017-4.
[46] S.H. Salleh, M.Z. Omar, J. Syarif, M.J. Ghazali, S. Abdullah, Z. Sajuri, *Int. J. Mech. Mater. Eng.*, 4 (2) (2009) 123–126.
[47] V. Kumar, R. Thirumurugan, Shanmugam, *Int. J. Mater. Res.*, 111 (9) (2020) 761–770, https://doi.org/10.3139/146.111938.
[48] S.C. Krishna, K.T. Tharian, K.V.A. Chakravarthi, A.K. Jha, B. Pant, *Metallogr. Microstruct. Anal.*, 5 (2) (2016) 108–115, https://doi.org/10.1007/s13632-016-0266-0.
[49] G. Prieto, A. Mandri, G. Rabbia, W.R. Tuckart, R. Dommarco, *J. Mater. Eng. Perform.*, 29 (4) (2020) 2216–2226, https://doi.org/10.1007/s11665-020-04777-y.
[50] S.C. Krishna, N.K. Karthick, A.K. Jha, B. Pant, P.V. Venkitakrishnan, *Metallogr. Microstruct. Anal.*, 6 (5) (2017) 425–432, https://doi.org/10.1007/s13632-017-0381-6.
[51] I. Pichard, D. Girodin, G. Dudragne, J.-Y. Moraux, A.S.T.M. Spec, *Tech. Publ.*, 1327 (1998) 391–405.
[52] M.A. Ragen, D.L. Anthony, R.F. Spitzer, A.S.T.M. Spec, *Tech. Publ.*, no. 1419 (2002) 362–374, https://doi.org/10.1520/stp10866s.

[53] O. Laurent, J. Bellus, S. Puech, F. Devilder, and A. Benbahmed, *ASTM Spec. Tech. Publ.*, vol. STP 1580, pp. 239–258, 2015, doi: 10.1520/STP158020140121.
[54] J.E. Andersson, F. Lindberg, and S. Ooi, "Hybrid steel and its potential for bearing applications," in *ASTM Special Technical Publication*, ASTM International, 2020, pp. 436–454. doi: 10.1520/STP162320190163.
[55] M. Hörnqvist Colliander, S. Ooi, K. Lindgren, T. Müller, M. Thuvander, *Metall. Mater. Trans. A Phys. Metall. Mater. Sci.*, (2024), https://doi.org/10.1007/s11661-024-07536-z.
[56] C. Örnek, B. Payam, A. Gloskovskii, K. Kazmanlı, N. Mohamed, B. Derin, M. Ürgen, C. E. Chou, H. W. Yen, B. Avcı, and S. Ooi, *npj Mater. Degrad.*, vol. 7, no. 1, 2023, doi: 10.1038/s41529-023-00392-z.
[57] S. Jakob, M. Hörnqvist Colliander, J. Kawser, S. Rashidi, S.W. Ooi, M. Thuvander, *Metall. Mater. Trans. A Phys. Metall. Mater. Sci.*, 55 (3) (2024) 870–879, https://doi.org/10.1007/s11661-023-07291-7.
[58] F. Aiello, M. Beghini, C. M. Belardini, L. Bertini, G. Macoretta, B. D. Monelli, and R. Valentini, *Corros. Sci.*, vol. 222, no. April, 2023, doi: 10.1016/j.corsci.2023.111357.
[59] P.G. Shewmon, *Mater. Sci. Technol. (united Kingdom)* 1 (1) (1985) 2–11, https://doi.org/10.1179/mst.1985.1.1.2.
[60] M.A.M. Alshahrani, S.W. Ooi, M.H. Colliander, G.M.A.M. El-Fallah, H.K.D. H. Bhadeshia, *Metall. Mater. Trans. A Phys. Metall. Mater. Sci.*, 53 (12) (2022) 4221–4232, https://doi.org/10.1007/s11661-022-06809-9.
[61] M.A.M. Alshahrani, S.W. Ooi, G. Divitini, H.K.D.H. Bhadeshia, *Int. J. Hydrogen Energy* 50 (2024) 189–198, https://doi.org/10.1016/j.ijhydene.2023.09.179.
[62] S. Wang, P. Zhang, M. Laleh, L. Jiang, M.Y. Tan, R.K.W. Marceau, *Npj Mater. Degrad.*, 8 (119) (2024) 1–13, https://doi.org/10.1038/s41529-024-00528-9.
[63] J. Takahashi, K. Kawakami, S. Teramoto, *Mater. Charact.*, 218 (P1) (2024) 114557, https://doi.org/10.1016/j.matchar.2024.114557.
[64] Z.H. Li, T.T. Sasaki, R. Ueji, Y. Kimura, A. Shibata, T. Ohkubo, K. Hono, *Scr. Mater.*, 241 (June) (2024) 2023, https://doi.org/10.1016/j.scriptamat.2023.115859.
[65] R. Niu, H. Li, P.Y. Liu, P. Burr, Y. Feng, H.W. Yen, C. Huang, Y.H. Sun, M. Ma, A. Guo, H. Lu, Y.S. Chen, J.M. Cairney, *Acta Mater.*, 281 (August) (2024) 120327, https://doi.org/10.1016/j.actamat.2024.120327.
[66] D. Hardie, S. Liu, *Corros. Sci.*, 38 (5) (1996) 721–733, https://doi.org/10.1016/0010-938X(96)00161-8.
[67] A. R. Troiani, R. Gibala, and R. F. Hehemann, *Hydrogen embrittlement and stress corrosion cracking: a Troiani Festschrift*, 6th ed. Ohio: American Society for Metals, 2002.,Ohio.
[68] W. Qin, J.A. Szpunar, *Philos. Mag.*, 97 (34) (2017) 3296–3316, https://doi.org/10.1080/14786435.2017.1378451.
[69] Z. Peng, J. Liu, F. Huang, S. Zhang, Q. Hu, Z. Wang, Y. Wang, *Int. J. Hydrogen Energy* 46 (56) (2021) 28811–28822, https://doi.org/10.1016/j.ijhydene.2021.06.096.
[70] X. Ren, W. Chu, J. Li, Y. Su, L. Qiao, *Mater. Chem. Phys.*, 107 (2–3) (2008) 231–235, https://doi.org/10.1016/j.matchemphys.2007.07.004.
[71] M.L. Martin, P. Sofronis, *J. Nat. Gas Sci. Eng.*, vol. 101, no. December 2021, p. 104547, 2022, doi: 10.1016/j.jngse.2022.104547.
[72] L.C.D. Fielding, E.J. Song, D.K. Han, H.K.D.H. Bhadeshia, D.W. Suh, R. Proc, A. Soc, *Math. Phys. Eng. Sci.*, 470 (2168) (2014) 32, https://doi.org/10.1098/rspa.2014.0108.
[73] S.D. Pu, A. Turk, S. Lenka, S.W. Ooi, *Mater. Sci. Eng. A* 754 (March) (2019) 628–635, https://doi.org/10.1016/j.msea.2019.03.098.
[74] M.J. Peet, T. Hojo, *Metall. Mater. Trans. A Phys. Metall. Mater. Sci.*, 47 (2) (2016) 718–725, https://doi.org/10.1007/s11661-015-3221-9.